# Numerical Analysis of Ignition Overpressure Effect on H-IIB Launch Vehicle

Seiji Tsutsumi[1] and Ryoji Takaki[2]
*Japan Aerospace Exploration Agency, Sagamihara, Kanagawa, 252-5210, Japan*

and
Toshiaki Hara[3], Hiroyuki Ueda[4], and Hiroyuki Nagata[5]
*Japan Aerospace Exploration Agency, Tsukuba, Ibaraki, 305-8505, Japan*

**A numerical simulation was conducted to investigate the ignition overpressure mechanism generated by the Japanese H-IIB launch vehicle. A simplified benchmark problem and analysis of a free jet exhausted from a single solid booster were used to verify the present numerical method; the unsteady Reynolds averaged Navier-Stokes simulation was found to be essential for determining the typical features of ignition overpressure, such as the shock wave generated in front of the plume and following starting vortex. Comparing with the measured pressure history at the launch complex, the numerical result agreed reasonably. The correlation between the wave pattern measured at the launch complex and the ignition overpressure mechanism was clarified. The effect of ignition overpressure on the launch vehicle can be reduced by shielding the inlet of the flame duct with a mobile launcher; however severe impact on the launch complex is unavoidable. The numerical technique and knowledge obtained in this study are applicable in the preliminary design of a launch pad to mitigate the impact of ignition overpressure.**

## Nomenclature

$D$ = nozzle exit diameter, m

$P$ = pressure, kPa

$P_a$ = ambient pressure, kPa

---

[1] Engineer, JAXA's Engineering Digital Innovation (JEDI) Center, 3-1-1 Yoshinodai, AIAA Member.
[2] Associate Professor, JAXA's Engineering Digital Innovation (JEDI) Center, 3-1-1 Yoshinodai, AIAA Member.
[3] Engineer, Space Transportation Mission Directorate, 2-1-1 Sengen.
[4] Associate Senior Engineer, Space Transportation Mission Directorate, 2-1-1 Sengen.
[5] Senior Engineer, Space Transportation Mission Directorate, 2-1-1 Sengen.

$P_o$ = stagnation pressure at nozzle inlet, kPa

$\Delta P$ = pressure fluctuation from ambient pressure, kPa

$T$ = time, s or ms

# I.  Introduction

AN intense pressure wave was observed around the launch pad of the Japanese H-IIB heavy launcher within 1 s after ignition of the solid boosters. The magnitude of the pressure wave measured at the acoustic insulation cover shown in Fig. 1 was roughly 20 kPa. The pressure wave was considered to originate from ignition overpressure (IOP). Ignition overpressure is an important factor to be considered in the design of a launch pad because of its impact on launch vehicles, payloads, and launch complexes. Therefore, much research is being devoted to it for the development of launch vehicles, such as the Ariane 5, and Ares I [1-10]. Only experimental and theoretical works from the early days of space development are available [1,2,4]. In the late 1990s, computational fluid dynamics (CFD) began being applied [3,5-7,9,11]. Both subscale experiments and CFD were recently used in the development process of the Ares I [8,9]. All previous studies based on CFD employed the conventional second-order method for both space and time evaluations [3,5-7,9,11]. Because the pressure wave of IOP wave has a large amplitude with low frequency compared with aeroacoustics, the second-order method may be sufficient for resolving the IOP. Ignition overpressure features are basically dominated by the inviscid features of fluid dynamics, so full Euler equations are used for the governing equations [5-7]. The unsteady Reynolds averaged Navier-Stokes (URANS) equations [3], hybrid RANS and large-eddy simulation (LES) [9], and pure LES [11] have also been employed in previous studies. The governing equations and turbulent models suitable for the practical simulation of IOP are not always clear. Because the physical time required to simulate IOP generation and propagation is of the order of 1 s, the computational model should be carefully chosen. Otherwise, the computational cost becomes too expensive for application in the design phase. This study aimed to establish a CFD technique that can simulate IOP with sufficient reliability and within acceptable computational cost in terms of industrial use. The computational method required for simulating IOP was first examined using simplified problems. The developed method was validated using H-IIB flight data, and was then applied to investigate the reason for the severe pressure fluctuation observed at the launch pad of the H-IIB.
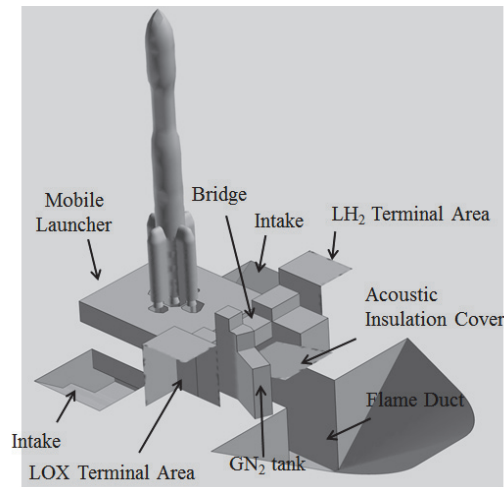
**Fig. 1 Computational model of launch complex.**

## II. Computational Model and Conditions

The launch complex of the H-IIB is shown in Fig.1. The engine plume enters into the flame duct located underneath the ground through the exhaust hole of the mobile launcher. The plume then goes downstream along the flame duct. The inlet of the flame duct is covered by the mobile launcher to shield the vehicle from IOP and acoustic waves radiated from the plume. Two intakes are attached to both sides of the flame duct. Launch complexes such as the LH$_2$/LOX terminal area, bridge, GN$_2$ tanks, and acoustic insulation cover are located at the ground surface. As shown in Fig. 2, the outer boundaries of the computational domain are located far enough to minimize the spurious wave reflected from the boundary. The computational mesh is shown in Fig.3. Based on the time-sequence diagram of the engine ignitions, the liquid engines located at the H-IIB core were concluded to be unrelated to IOP. Therefore, the exhaust plume from the two liquid engines at the center were omitted in the present study to lower the computational cost. As shown in Fig. 3(a), a hexahedral mesh was generated to resolve the plume of the four solid boosters. A tetrahedral mesh was placed around the hexahedral mesh to cover the launch complexes, as shown in Fig. 3(b). The total number of mesh elements was $8.7 \times 10^6$.

The plume from the solid booster was assumed to have a mixed gas composition in the chamber. The mixed gas was evaluated using a one-dimensional chemical equilibrium solver [12]. The mixed gas was imposed on the nozzle inlet with the time history of the chamber pressure obtained from the H-IIB flight. The stagnation temperature was

assumed to be constant, because it is only slightly sensitive to changes in the chamber pressure. Roughly 1 s was required to achieve a nominal chamber pressure.
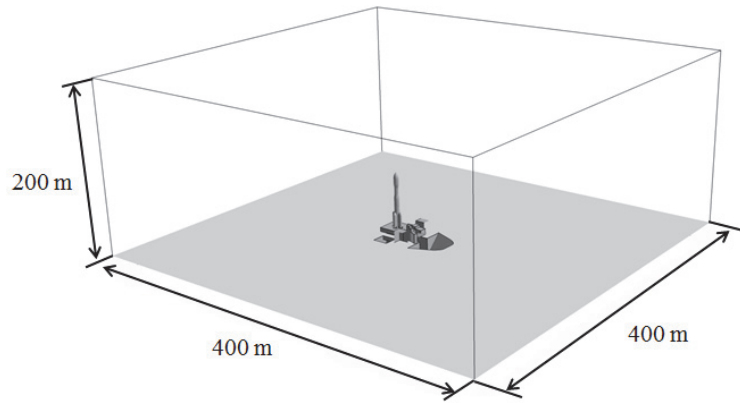


**Fig. 2  Computational region.**
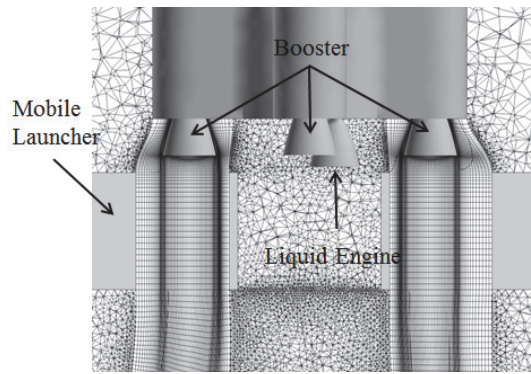


**(a) Close-up view at engines.**
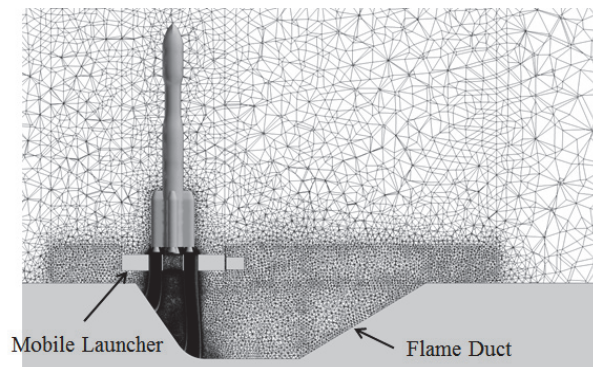


**(b) Symmetry plane.**
**Fig. 3  Computational mesh.**

## III. Numerical Method

As noted earlier, the physical time required to simulate IOP generation and propagation was about 1 s. The computational model should be carefully selected to lower the computational cost. In this study, the commercial CFD software CFD++ Ver.11.1.1 (Metacomp Technology, Inc.) was employed. CFD++ is based on an unstructured mesh, and second-order accuracy can be achieved in both space and time. The notable feature of this commercial CFD software is the wide variety of computational models. Therefore, the commercial software was attractive, since it is still unclear what type of governing equations and turbulence model are appropriate for IOP simulation. In this study, two chemical species were considered: the ambient air and the plume from the solid boosters. As noted earlier, the plume was assumed to have a mixed gas composition in the chamber. Chemical reactions were not considered, so the effect of exhaust plume afterburning was neglected. The numerical flux for convective terms was evaluated using the Harten-Lax-van Leer-Contact (HLLC) Riemann solver. Second-order spatial accuracy was achieved using monotonic upwind schemes for conservation laws (MUSCL) interpolation. The point implicit time integration method was used with a second-order three-point backward differential formula with Newton-Raphson sub-iterations. The selection of the governing equations and turbulence model is discussed in the next section. The inflow boundary condition at the nozzle inlet was determined using the prescribed time-dependent stagnation pressure, constant stagnation temperature, and velocity components extrapolated from interior cells. Most launch pads, including that of the H-IIB, are equipped with a water injection system for IOP attenuation. The possible effects of water injection are discussed in the references, [1] but it is not realistic to model all these effects in CFD for application in a practical configuration. Therefore, this study omitted water injection.

First, CFD++ was applied to a two-dimensional IOP wave propagation problem, [13,14] and code-to-code comparison was performed as part of the verification study. Three-dimensional Euler equations were employed for this benchmark problem. As a comparison, results using JAXA's in-house CFD software UPACS-2.0 [15] were obtained. As shown in Fig. 4, the benchmark problem consisted of a two-dimensional supersonic nozzle located above a 45° inclined flat plate. The exit Mach number of the nozzle was 2.0. The distance between the nozzle and inclined plate was five times longer than the nozzle exit diameter, D. The stagnation pressure at the nozzle inlet, Po, ramped up linearly, as shown in Fig. 5. Details on the benchmark problem and mesh refinement study are given in the references [13,14]. Snapshots of the static pressure plot obtained by CFD++ are shown in Fig. 6. The Mach number contour line is superimposed on these figures to emphasize the jet flow. Fig. 6(a) (T = 4 ms) shows that the pressure

in front of the jet increased due to the formation of the shock wave. Following the formation of the shock wave, low-pressure regions formed at both sides of the nozzle lip because of the starting vortex [16]. The jet, shock wave, and starting vortex moved downstream along the inclined plate and is shown at T = 9 ms in Fig. 6(b). At T = 14 ms (Fig. 6(c)), a pressure wave having a circular curvature was observed behind the starting vortex. The pressure wave radiated from the nonphysical flapping of the unresolved jet shear layer in the present numerical setup. The time histories of the static pressure at the sampling point shown in Fig. 4 were compared, as shown in Fig. 5. The pressure started to increase at 1 ms due to the shock wave. The pressure then decreased at roughly 4 ms because of propagation of the starting vortex. A comparison of the UPACS-2.0 and CFD++ results showed reasonable agreement at T < 9 ms until a spurious pressure wave begins to move through the sampling point. Afterwards, both results showed small fluctuations with slight differences. The fluctuations originated from the spurious pressure wave due to the unresolved jet shear layer as shown in Fig. 6(c). In terms of the positive and negative pressure fluctuation due to IOP, however, reasonable agreement was obtained. Therefore, CFD++ was employed in the following evaluation.
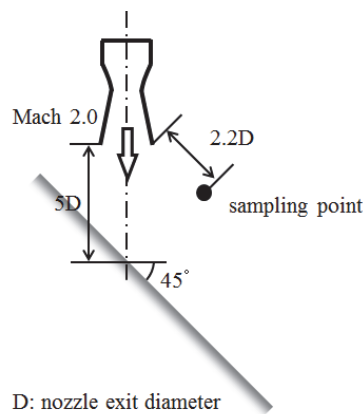


**Fig. 4  Schematic of two-dimensional IOP test problem.**
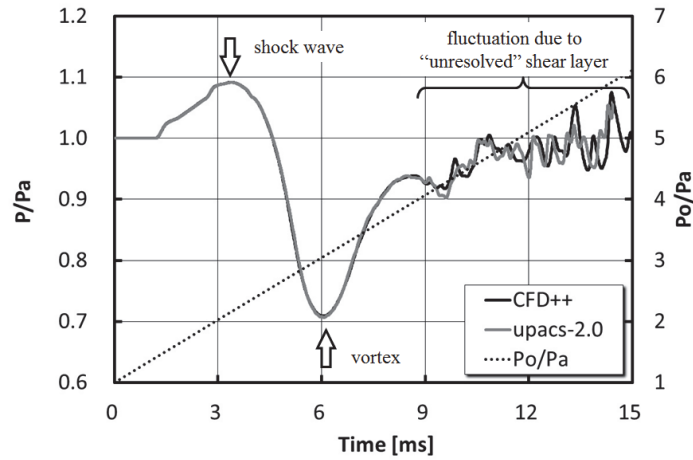
**Fig. 5  Time histories of stagnation pressure at nozzle inlet and static pressure at sampling point. Location of sampling point is indicated in Fig. 4.**



**(a) T=4 ms.**          **(b) T=9 ms.**          **(c) T=14 ms.**
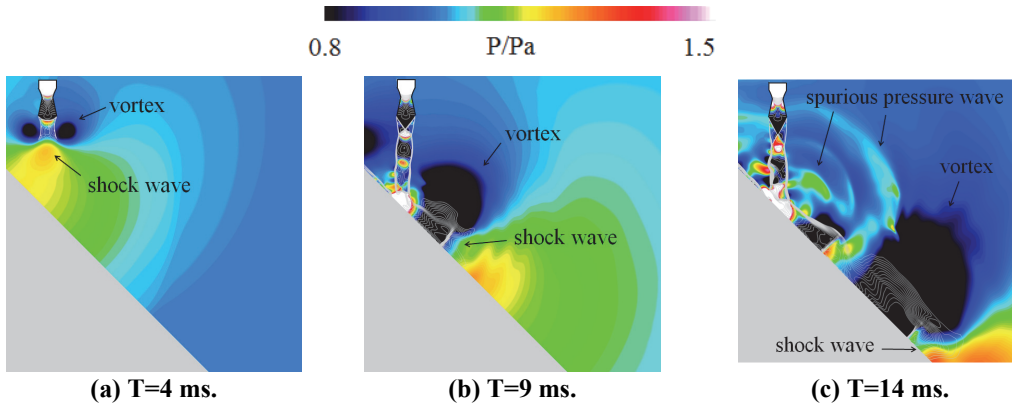
**Fig. 6  Time-series static pressure plots obtained using CFD++. Jet is represented by white-colored Mach number contour line.**

## IV.    IOP Simulation Generated from Free Jet of Single Solid Booster

As discussed in the previous section, the governing equations and turbulence model required for IOP analysis have not been clarified. A free jet exhausted from a single solid booster was numerically simulated using the two setups listed in Table 1. The governing equations for the first case (i.e., "Euler") were the three-dimensional Euler equations. Unsteady three-dimensional Reynolds-averaged Navier-Stokes (URANS) equations were employed for the second case (i.e., "URANS"). The eddy viscosity was modeled using the realizable k-ε model. A wall function was applied to model the turbulence boundary layer on a solid wall to relax the time step restriction there. As shown in Table 1, the time step of the Euler case was 2.5 times larger than that of the URANS case. The number of Newton-Raphson

sub-iterations was individually chosen in those two cases to guarantee a residual drop of two orders of magnitude. Snapshots of the flowfield represented by the pressure and Mach number plots were compared in Fig. 7. Streamlines were superimposed on the pressure plots. Result of the URANS based on coarse grid was also shown in Fig.7 for grid convergence study that was discussed later in this section. The pressure plots of both cases showed that high- and low-pressure regions appeared side-by-side at around 30 m downstream from the nozzle exit. A comparison with the Mach number plots showed that the high-pressure region was located in front of the plume. The streamline indicates the existence of the starting vortex at the low-pressure region. Therefore, both the Euler and URANS cases showed the typical IOP features. Figure 8 compares the time histories of the pressure values obtained using the Euler and URANS equations. The sampling point indicated in Fig. 7 by a black circle was located 30 m downstream of the nozzle exit. A comparison of Figs. 7 and 8 showed that the first peak observed in the Euler case at T=0.03 s corresponded to the shock wave, and the dip in the pressure profile around T = 0.05 s stemmed from the vortex convection. The same feature was observed in the results of the URANS case, although the timing of IOP was different. In the Euler case results, another notable pressure peak formed at T = 0.09 s. The magnitude of the pressure fluctuation, $\Delta P$, was over 30 kPa, which is quite high compared to that of the IOP. A small pressure fluctuation was observed after T = 0.1 s in the Euler simulation, while a relatively flattened profile was obtained for the URANS case at the analogous time (after T = 0.2 s). Because the pressure peak observed in an H-IIB having four solid boosters was about 20 kPa, the pressure peak observed in the Euler case at T = 0.09 s was much higher than in practical. The Mach number plot of the URANS case (Fig. 7(b)) shows that no separation occurred inside the nozzle. The plume in the Euler case (Fig. 7(a)) showed unsteady motion around the nozzle exit, which led to the pressure wave propagating obliquely downstream. Because of the lack of viscosity in the Euler case, nonphysical separation occurred inside the nozzle, and unsteady motion of the plume was formed. The unsteady motion had high energy at low frequencies due to the insufficient spatial resolution, so a spurious acoustic wave of notable magnitude was radiated. Note that the two-dimensional benchmark problem described in section III employs the Euler equations, but such a spurious pressure wave was negligibly small, as shown in Fig. 5. Because the area ratio of the nozzle employed in the benchmark problem was lower, severe separation of the internal nozzle flow did not occur, and the spurious pressure wave radiated from the jet with a flapping motion was not so intense. Therefore, the turbulence model can be concluded to be essential when a nozzle having a high area ratio is considered in practice.

A mesh refinement study was conducted using the URANS CFD simulation. Results shown in the above discussion used a mesh of $1.9\times10^5$ cells. Coarse mesh having $4.2\times10^4$ cells was employed for the comparison. The flowfield was compared in Figs. 7(b) and 7(c). This comparison showed that, in general, the flowfield remained the same and consisted of a shock wave in front of the plume and a starting vortex behind the shock wave. The time histories of the static pressure were compared in Fig.8. Characteristics of the pressure profile were almost identical, although the $\Delta$P of the coarse mesh was lower than that of the fine mesh by roughly 10% and the timing of the shock wave and the vortex was slightly different. The comparison here showed that the coarse mesh had enough resolution within the qualitative discussion.

**Table 1    List of computational cases.**

|  | Gov. Eqns. | Turb. Model | $\Delta$T [ms] |
|---|---|---|---|
| Euler | 3D Euler | - | 0.25 |
| URANS | unsteady 3D Reynolds-averaged Navier-Stokes | Realizable k-ε w/ wall function | 0.1 |
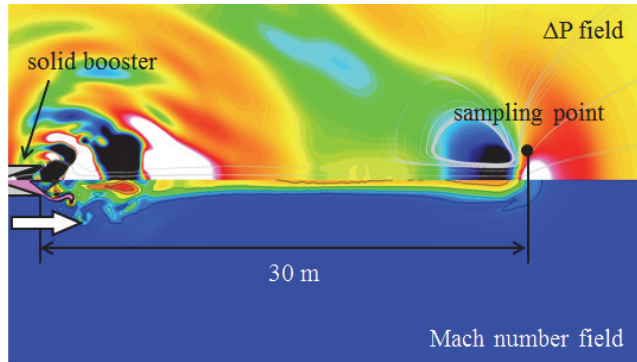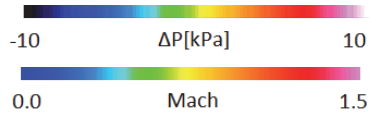
(a) Euler, T=0.04 [s].
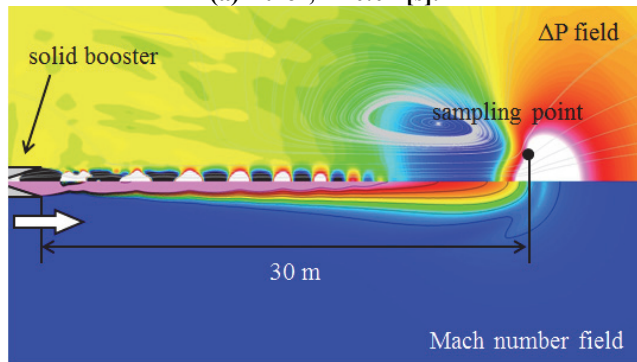
(b) URANS, T=0.12 [s].
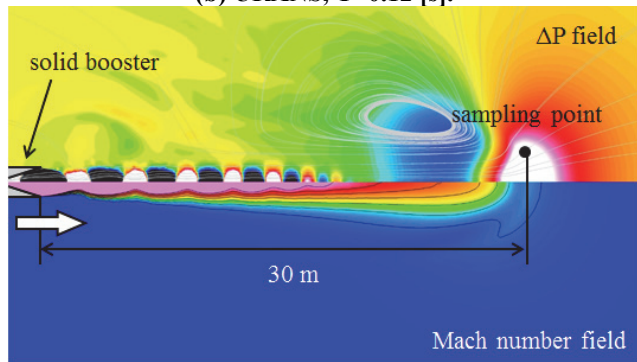
(c) URANS (coarse), T=0.12 [s].

Fig. 7  Comparison of flowfields. Upper: pressure plot, Lower: Mach number plot. Streamline is superimposed on the pressure plot.
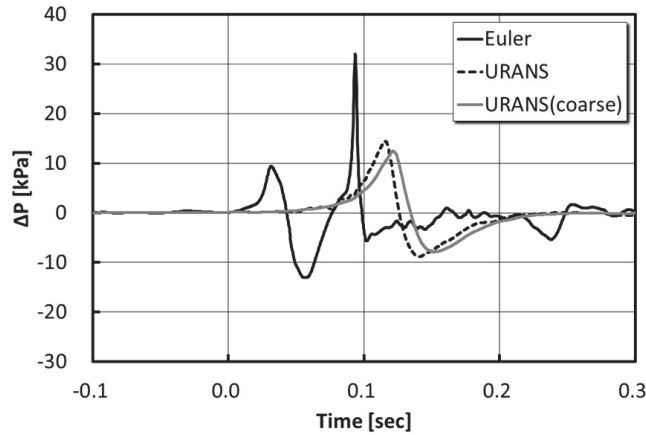
**Fig. 8 Time history of static pressure at sampling point shown in Fig. 7.**

## V.    Discussion on IOP Propagation at H-IIB

As discussed in section IV, the employed computational model was set to the URANS case. Details are presented

in Table 1. The computational mesh is shown in Fig.3. The mesh spacing at the region between the nozzle and the

flame deflector where the shock wave and vortex were formed was determined based on the coarse mesh used in the

IOP simulation generated from the free jet of a single solid booster. At the downstream side of the flame duct, the

mesh spacing was about 4 times larger than that of the coarse mesh. As observed in Fig. 7(b) and (c), the size of the

vortex that appeared in the free jet of a single solid booster was roughly 8 times as large as the nozzle exit diameter.

As a result, the computational mesh shown in Fig.3 was guaranteed to have 15 to 20 isotropic tetrahedral cells inside

cross-section of the vortex having two-dimensional shape. The mesh size at the downstream side of the flame duct

was enough to resolve the vortex propagation by using the present method having second-order spatial accuracy. The

solid boosters were ignited approximately 0.3 s before lift-off, and it took about 1 s for an IOP wave to be generated

and propagate across the launch pad according to the flight data. Therefore, the flowfield over an elapsed time of at

least 1 s should be simulated. Because the time step was 0.1 ms as shown in Table 1, 10,000 steps were required; the

computational time resulted in 256 cores of the JAXA's supercomputer Fujitsu FX1 being used for 12 days. The time

history of the pressure measured inside the acoustic insulation cover (see Fig. 1) was compared with the numerical

results presented in Fig. 9. The horizontal axis of Fig. 9 corresponds to the time based on lift-off. In the numerical

results, positive and negative peaks appeared at T = 0.18 s and 0.3 s, respectively. In the flight data, the positive peak

bifurcated at T = 0.12 s and 0.23 s, and the negative peak formed at around T = 0.3 s. Except for the bifurcation of the

positive peak in the flight data, the numerical results agreed reasonably with the flight data. The difference in the positive peak was attributed to the lack of plume ejected from the two liquid engines, the lack of a water injection system in the numerical model, or the lack of the afterburning effect as described earlier. To analyze the correlation with IOP propagation, time-series static-pressure plots with a density contour line at the symmetry plane were drawn, as shown in Fig. 10. At T = 0.1 s, a shock wave formed along the downstream side of the solid booster. As shown in Figs. 10(b) and (c), the shock wave propagated downstream with time. Figure 11 shows a three-dimensional shock wave structure visualized by the iso-surface of $\Delta P$ = +10 kPa at T = 0.2 s. The shock was found to be almost two-dimensional and filled the straight pathway of the flame duct. Because of shock wave generation and propagation, a high-pressure region formed and propagated downstream together with the shock wave, as shown in Fig.10. The high-pressure region corresponds to the positive pressure peak measured at around T = 0.1 s in Fig. 9. The starting vortex formed behind the shock wave. As shown in Fig. 10(b), the starting vortex was observed to be where the plume of the solid booster on the downstream side impinged the flame deflector at T = 0.2 s. As time advanced, the vortex structure convected downstream as its size increased. At T = 0.3 s (Fig. 10(c)), the flame duct was filled with the low-pressure region and was related to the negative pressure peak observed at around T = 0.3 s, as shown in Fig.9. The three-dimensional structure of the starting vortex at T = 0.2 s and 0.3 s is visualized by the streamline in Fig. 12. In the straight pathway of the flame duct, the starting vortex showed a two-dimensional shape. Because the flame duct was covered by the mobile launcher, the effects of the shock wave and starting vortex were shielded, as shown in Figs. 10(b) and 10(c). Therefore, IOP is not a serious issue with respect to the H-IIB launch vehicle. However, the IOP and resultant positive and negative pressure regions directly impinged on the downstream side of the launch complex, and the effect should not be neglected. Therefore, the structural design of the acoustic insulation cover must consider the impact of such severe pressure. The pressure difference between the flame duct and ambient air also induced a high-speed jet at the small gap between the launch complexes. Figure 12(a) shows that the streamline turned outward through the gap around the acoustic insulation cover because the static pressure inside the acoustic insulation cover was higher than that of the ambient air at T = 0.2 s due to the shock wave, as seen in Fig. 10(b). The velocity field at the symmetry plane is shown in Fig. 13. At T = 0.2 s, a jet with a flow velocity higher than 100 m/s was ejected outside through the gap between the acoustic insulation cover and bridge. At T = 0.3 s, the starting vortex was filled with the flame duct (Fig. 10(c)), so a complicated flow structure formed around the acoustic insulation cover. As shown in Fig. 12(b), a vortex structure appeared downstream of the acoustic insulation cover, while outside air was entrained through

the small gap upstream. As shown in Fig. 13(b), the jet entrained inside through the small gap between the acoustic insulation cover and bridge also had a flow velocity higher than 100 m/s. Such high-speed jets may be able to severely damage the launch complex. The results obtained in this study indicate the importance of understanding IOP propagation and the resultant pressure fields as well as the need for launch pad design that minimizes the impact of IOP on vehicles, payloads, and launch complexes.
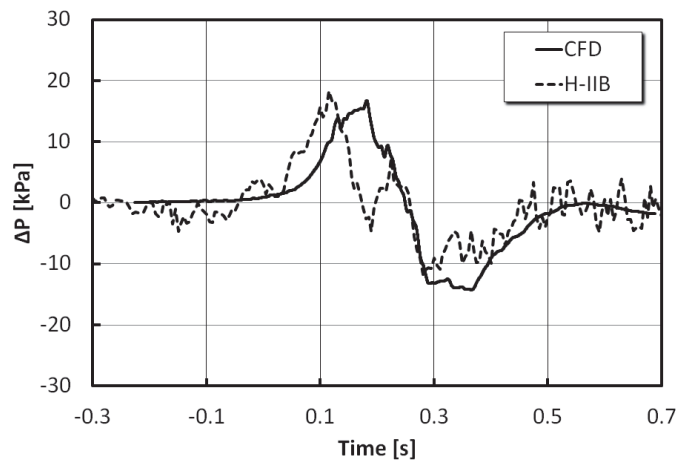


**Fig. 9 Comparison of numerical result with H-IIB flight data measured at acoustic insulation cover.**



**(a) T=0.1 s.** **(b) T=0.2 s.**
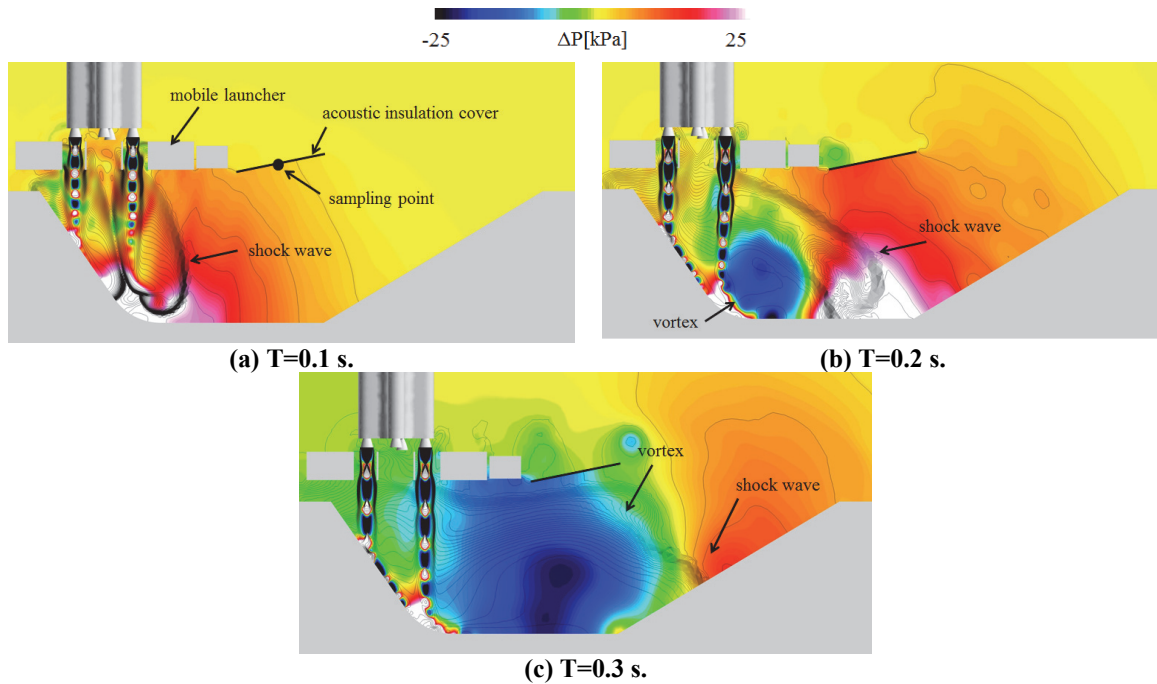


**(c) T=0.3 s.**
**Fig. 10    Time-series static pressure plots with density contour line.**
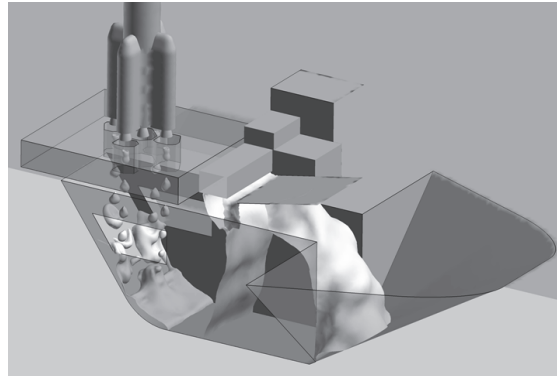
**Fig. 11    Shock wave structure visualized by iso-surface of ΔP=+10 kPa at T=0.2 s.**



0            Vel. Mag. [m/s]            100
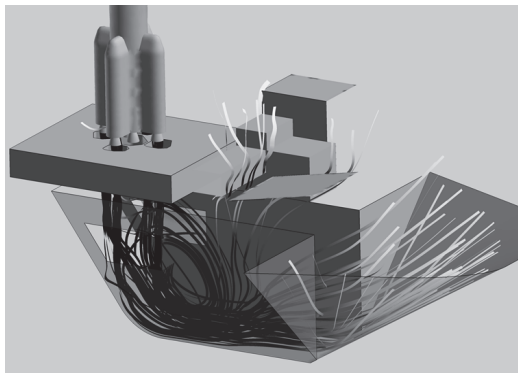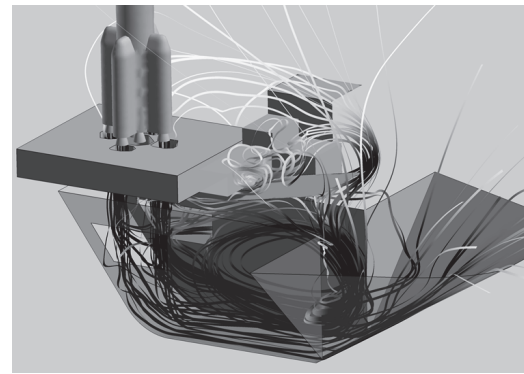
**(a) T=0.2 s.**                                    **(b) T=0.3 s.**
**Fig. 12    Streamline painted with velocity magnitude.**



0            Vel. Mag. [m/s]            100

Mobile Launcher

Bridge

Acoustic Insulation Cover
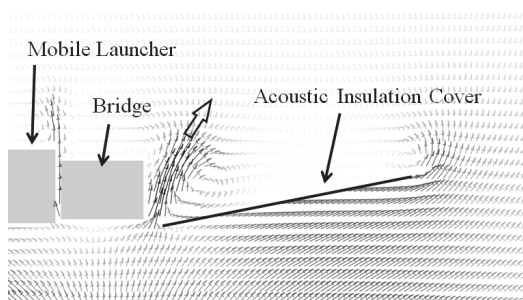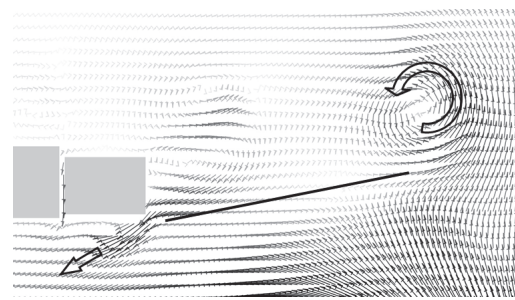
**(a) T=0.2 s.**                                    **(b) T=0.3 s.**

**Fig. 13    Velocity field at the symmetry plane of mobile launcher and acoustic insulation cover.**

# VI.   Conclusion

An intense pressure wave was observed around the launch pad of the Japanese H-IIB launch vehicle within 1 s after ignition of the solid boosters. The pressure wave was considered to originate from ignition overpressure. This study aimed to establish a numerical technique that can simulate ignition overpressure with sufficient reliability and low computational cost to meet the requirements of industrial use. A two-dimensional benchmark problem was simulated first. The present numerical technique was verified through code-to-code comparison. The numerical technique was then applied to the free jet exhausted from the single solid booster. The numerical simulation based on the Euler equation found a spurious pressure wave coming from the flapping motion of the plume. An unsteady Reynolds averaged Navier-Stokes simulation using the realizable k-ε model with a wall function was applied, and typical features of ignition overpressure, such as a shock wave forming in front of the plume and the starting vortex, were reasonably observed. The numerical technique was then applied to the practical launch configuration of the H-IIB launcher. The numerical result agreed reasonably well with the time history of the pressure obtained during the actual flight. The positive pressure peak observed in the flight data was found to be caused by the shock wave generated at the plume of the solid boosters. Convection of the starting vortex caused the negative pressure peak in the flight data. Because the flame duct was covered by the mobile launcher, the effect of ignition overpressure was mitigated and was therefore not a serious risk to the launch vehicle. However, ignition overpressure and the resultant pressure fluctuation directly impinge the launch complex, so the effect should not be neglected.

The present numerical method based on the unsteady Reynolds averaged Navier-Stokes simulation is applicable to the preliminary design of a launch pad. In addition, knowledge about ignition overpressure obtained in this study is helpful to mitigate the impact of ignition overpressure.

## References

[1] Ryan, R.S., Jones, J.H., Guest, S.H., Struck, H.G., Rheinfurth, M.H., and Verderaime, V.S., "Propulsion System Ignition Overpressure for the Space Shuttle," NASA TM-82458, 1981.

[2] Ikawa, H., and Laspesa, F.S., "Ignition/Duct Overpressure Induced by Space Shuttle Solid Rocket Motor Ignition," *Journal of Spacecraft and Rockets*, Vol. 22, No. 4, 1985, pp. 481-488.

[3] Kiris, C.C., Chan, W., Housman, Kwak, D., and Housman, J., "Time-Accurate Computational Analysis of the Flame Trench", *Computational Fluid Dynamics 2008*, 2009, pp. 261-267.

[4] Walsh, E.J., and Hart, P.M., "Liftoff Ignition Overpressure – A Correlation," *Journal of Spacecraft and Rockets*, Vol. 19, No. 6, 1981, pp. 550-556.

[5] Salita, M., and Glatt, L., "Modeling of Ignition Overpressure in Minuteman Silos," AIAA 1997-2720, 1997.

[6] Pavish, D.L., and Deese, J.E., "CFD Analysis of Unsteady Ignition Overpressure Effects on Delta II and Delta III Launch Vehicles," AIAA 2000-3922, August, 2000.

[7] Canabal, F., and Frendi, A., "Study of the Ignition Overpressure Suppression Technique by Water Addition," *Journal of Spacecraft and Rockets*, Vol. 43, No.4, 2006, pp.853-865.

[8] Casiano, M.J., Alvord, D.A., and McDaniels, D.M., "Ares I Scale Model Acoustic Test Overpressure Results," NASA TM-2011-217452, 2011.

[9] Putnam, G.C., and Strutzenburg, L.L., "Simulation of Acoustics for Ares I Scale Model Acoustics Tests," *Journal of Acoustical Society of America*, Vol. 130, No. 4, 2011, pp. 2543.

[10] Troclet, B., Alestra, S., Terrasse, I., Jeanjean, S., and Srithammavanh, "Identification of Overpressure Sources at Launch Vehicle Lift-off Using an Inverse Method," European Conference for Aerospace Sciences, 1.02.07, July, 2005.

[11] Troyes, J, Vuillot, F., Varnier, J., and Malbequi, P., "Numerical Simulations of Rocket Solid Motor Engine Ignition and Duct Overpressure Waves at Reduced Scale," AIAA 2009-4981, 2009.

[12] Gordon, S., and McBride, B.J., "Computer Program for Calculation of Complex Chemical Equilibrium Compositions and Applications," NASA RP-1311, 1994.

[13] Nonomura,T., Tsutsumi, S., Takaki, R., Shima, E., and Fujii. K., "Impact of Spatial and Temporal Resolution on the Aeroacoustic Wave from a Two-dimensional Impinging Jet," 7th International Conference on Computational Fluid Dynamics, ICCFD7-3103, 2012.

[14] Housman, J.A., Barad, M.F., and Kiris, C.C., "Space-Time Accuracy Assessment of CFD Simulations for the Launch Environemnt," AIAA Paper 2011-3650, June, 2011.

[15] Takaki, R., Yamamoto, K., Yamane, T., Enomoto, S., Mukai, J., "The Development of the UPACS CFD Environment," High Performance Computing, Lecture Notes in Computer Science, Vol. 2858, 2003, pp. 307-319.

[16] Auerbach, D., "Experiments on the Trajectory and Circulation of the Starting Vortex," *Journal of Fluid Mechanics*, Vol. 183, 1987, pp. 185-198.